Evolution of the Josephine Peridotite shear zones, Part 2: Influences on olivine CPO evolution

Kathryn M. Kumamoto[1,2*], Jessica M. Warren[3], and Lars N. Hansen[1]

[1] Department of Earth Sciences, University of Oxford, UK.

[2] Department of Geological Sciences, Stanford University, CA.

[3] Department of Geological Sciences, University of Delaware, DE.

[*] Corresponding author

Key points:

- Olivine CPO evolution is not clearly linked to strain or water content in Josephine Peridotite shear zones.
- Variability in CPO at low strain can be explained by the effect of a pre-existing CPO.
- Texture modeling suggests E-type CPOs at high strain can be explained by kinematics involving a combination of simple shear and pure shear.

Abstract

Seismic anisotropy arises in the upper mantle due to the alignment of olivine crystal lattices and is often used to interpret mantle flow direction. Experiments on the evolution of olivine crystal-preferred orientation (CPO) have found that the texture that develops is dependent on many factors, including water content, differential stress, pre-existing CPO, and deformation kinematics. To evaluate the role of these factors in naturally deformed samples, we present microstructural transects across three shear zones in the Josephine Peridotite. Samples from these shear zones exhibit a mixture of A-type textures, which have been associated with dry conditions and primary activation of the olivine [100](010) slip system, and of E-type textures, which have been associated with wetter conditions and primary activation of the [100](001) slip system. CPOs with characteristics of both A-type and E-type textures are also present. CPO type does not evolve systematically as a function of either strain or water content. We used a micromechanical model to evaluate the roles of pre-existing texture and kinematics on olivine CPO evolution. We find that the pre-existing texture controls CPO evolution at strains up to 5 during simple shear. Kinematics involving a combination of simple shear and pure shear can explain the olivine CPOs at higher strain. Hence, pre-existing CPOs and deformation kinematics should be considered in the interpretation of CPOs measured in naturally deformed rocks and of large-scale patterns in upper-mantle seismic anisotropy.

1. Introduction

Mantle seismic anisotropy results from the alignment of olivine crystal lattices during flow at high-temperature in the upper mantle, with the crystal-preferred orientation (CPO) of olivine evolving in response to strain (e.g., Hess, 1964; Nicolas et al., 1973; Nicolas & Christensen, 1987). Different CPOs arise from the dominance of different slip systems and have been used to interpret deformation conditions (e.g., Ben Ismaïl & Mainprice, 1998; Jung & Karato, 2001). The most common CPO observed in upper mantle peridotites is created by slip predominantly in the [100] direction on the (010) plane (e.g., Tommasi et al., 2000) and is often referred to as A-type (Figure 1). Experimental and theoretical studies have proposed that olivine CPO is a function of differential stress and water content (e.g., Jung et al., 2006; Jung & Karato, 2001; Katayama et al., 2004), as well as other parameters such as melt content (e.g., Holtzman et al., 2003; Qi et al., 2018), confining pressure (e.g., Mainprice et al., 2005), temperature (e.g., Katayama & Karato, 2006), pre-existing CPO (e.g., Boneh & Skemer, 2014; Hansen, Warren, et al., 2016), and deformation kinematics (e.g., Tommasi et al., 1999).

At the low differential stresses (~10 MPa) inferred for flow in the uppermost mantle (e.g., Behr & Hirth, 2014; Chin et al., 2016; Hansen & Warren, 2015), a water-induced transition between texture types is predicted by simple shear experiments at a few hundred ppm H/Si in olivine (e.g., Jung et al., 2006; Katayama et al., 2004), from an A-type texture to an E-type texture associated with slip in the [100] direction on the (001) plane (Figure 1). However, recent studies by Bernard and Behr (2017) and Bernard et al. (2019) on continental mantle xenoliths revealed no discernable relationship between water concentration and these CPO types. Unfortunately, interpretation of CPOs from xenoliths is often difficult due to poor constraints on deformation conditions, including shear plane and shear direction orientations, deformation kinematics, and shear strains.

To clarify the factors controlling variation in olivine CPO, observations are needed in peridotite outcrops (e.g., orogenic massifs and ophiolites) for which the field context can provide constraints on deformation conditions. Additional factors in CPO evolution can then be considered, including the presence and orientation of a pre-existing CPO and the kinematics of deformation. Pre-existing CPOs can have a large effect on the rate of CPO evolution as well as the texture types attained at low strains (e.g., Boneh & Skemer, 2014; Hansen et al., 2012; Hansen, Warren, et al., 2016). Different deformation kinematics (i.e., non-simple shear) also strongly affect texture development, based on both modeling (e.g., Tommasi et al., 1999) and deformation experiments (e.g. Hansen, Warren, et al., 2016). In addition, experiments utilizing triaxial compression and thus kinematics similar to pure shear (e.g., Boneh & Skemer, 2014; Hansen et al., 2011) result in CPOs significantly different from experiments utilizing torsion and thus simple shear kinematics (e.g., Bystricky et al., 2000; Hansen et al., 2014).

Here, we explore the link between olivine CPO, water content, and deformation kinematics in shear zones in the Fresno Bench outcrop of the Josephine Peridotite in southwestern Oregon (e.g., Kelemen & Dick, 1995; Loney & Himmelberg, 1976; Skemer et al., 2010; Warren et al., 2008). We find that samples with different olivine CPOs have similar water contents, suggesting that water was not the main factor controlling CPO formation in these shear zones. We use a textural evolution model (Hansen, Conrad, et al., 2016) to evaluate the roles of a pre-existing CPO and complex deformation kinematics on the evolution of olivine CPOs in the Fresno Bench shear zones, and our results indicate that many of the features observed in the olivine CPOs of the Fresno Bench shear zones can be explained by a combination of these two factors.

2. Geological setting

The Josephine Peridotite (Figure 2) is the mantle section of a 150 Ma ophiolite exposed in the Klamath Mountains of southwestern Oregon (Garcia, 1982; Harper, 1984; Saleeby et al., 1982). This study focuses on Fresno Bench, an outcrop with an area of <1 km^2 in the 640 km^2 exposure of peridotite (Dick, 1977; Himmelberg & Loney, 1973). Fresno Bench is notable in that numerous small shear zones are exposed (Figure 2), ranging from centimeters to tens of meters in width (Kelemen & Dick, 1995; Loney & Himmelberg, 1976; Nevitt et al., 2019; Skemer et al., 2010; Warren et al., 2008). The peridotite in this area exhibits near-ubiquitous layering of pyroxene-rich and pyroxene-poor harzburgite. These layers are deflected by shear-zone deformation, from a sub-horizontal orientation present across the majority of the outcrop to a sub-vertical orientation at the center of each shear zone. The shear zones are estimated to have formed in the shallow mantle at <30 km depth and temperatures of 900-1200˚C, based on major element geothermometry of the peridotite and syndeformational gabbroic dikes (Harding, 1988; Kelemen & Dick, 1995; Kumamoto et al., in revision; Loney & Himmelberg, 1976; Skemer et al., 2010).

Here, we examine three of the best-exposed Fresno Bench shear zones: Shear Zone P (SZP; Hansen & Warren, 2015; Warren et al., 2008), Shear Zone G (SZG; Skemer et al., 2010), and Shear Zone A (SZA; Recanati et al., 2012). All three shear zones are predominantly harzburgite, though the harzburgite in SZP is interlayered with dunite. The strike of the vertical shear plane in each shear zone was determined from the orientation of the pyroxene foliation with the steepest dip. Shear strain was determined using the deflection of the pyroxene foliation at each point relative to the orientation of the foliation at the edge of the shear zone (following Ramsay & Graham, 1970, and Warren et al., 2008). Longer discussions of shear strain measurements and geochemical measurements for these shear zones are presented in a companion study on the melt interaction history of the Fresno Bench shear zones (Kumamoto et al., in revision).

3. Microstructural analysis

Electron backscatter diffraction (EBSD) was used to measure olivine orientations and grain size in a transect of 9 samples across SZA. Microstructures and CPOs for SZG and SZP transects have previously been published (Hansen & Warren, 2015; Skemer et al., 2010; Warren et al., 2008). Two additional SZG samples and three additional SZP samples were analyzed to provide grain size estimates following the same methodology used here and previously for SZP (Hansen & Warren, 2015). For EBSD analysis, oriented thin sections were polished using diamond solutions down to a grit size of 0.25 µm, followed by 0.06 µm colloidal silica. Samples from SZA were analyzed using AZtec 2.0 software on an FEI Quanta 200 scanning electron microscope with an Oxford Instruments NordlysF EBSD detector and an X-max 20 mm^2 silicon drift detector at the Department of Plant Biology, Carnegie Institution of Washington. Samples from SZG and SZP were analyzed using AZtec 3.3 software on a Zeiss Auriga 60 with an Oxford Instruments NordlysF EBSD detector at the University of Delaware. Step sizes varied between 7.5 and 20 µm, all sufficiently small to resolve olivine grain sizes in these samples. A minimum of 200 grains of olivine per sample were measured to ensure that the CPO and grain size in the map were representative of the sample.

EBSD data were processed using the Channel5 software package to perform noise reduction, remove systematic misindexing, create phase maps, and measure grain size. Noise reduction included the use of the Kuwahara filter to improve resolution of low-angle misorientations (Humphreys et al., 2001). In comparing Channel5 and MTEX (Bachmann et al., 2010; Mainprice et al., 2014) routines for calculating misorientation inverse pole figures (MIPFs), we found that applying this filter was essential to producing consistent results between the two programs. Average grain size and subgrain size were measured using the linear intercept method along lines parallel and perpendicular to the shear direction, using the arithmetic mean and a geometric correction factor of 1.5 to obtain an estimate of the mean 3D grain size from a 2D cross-section (Hansen & Warren, 2015; Underwood, 1970, pp. 80–93). Critical angles for these two measurements were set at 10˚ and 1˚, respectively. The MTEX package for MATLAB (Bachmann et al., 2010; Mainprice et al., 2014) was used to create and analyze crystal orientation pole figures as well as low-angle MIPFs, with orientation distribution functions for each sample calculated using a kernel half-width of 10˚. Measurements of the texture strength, the J-index (Bunge, 1982) and M-index (Skemer et al., 2005), were also calculated using MTEX. Eigenvalue analysis (Woodcock, 1977) was used to calculate the average orientation of each crystallographic axis in each CPO. This analysis was also used to calculate the shape parameter, K, for the orientation distribution of each crystallographic axis as:

$$K_{hkl} = \frac{\ln(S_1/S_2)}{\ln(S_2/S_3)} \quad (1)$$

where S_1, S_2, and S_3 are the first, second, and third eigenvalues, respectively, for that distribution (Woodcock, 1977). K is a representation of clustering in the data. Values of $0<K<1$ represent a girdled texture, and values of $K>1$ represent a point maximum.

4. Results

4.1. Olivine textural evolution

We evaluated the microstructures of 9 harzburgite samples from SZA, 11 harzburgite and 6 dunite samples from SZP, and 2 harzburgite samples from SZG, for a total of 28 samples. The results are summarized in Tables 1 and S1. In Figures 3–5 and Figure S1, EBSD data of olivine are plotted relative to the structural reference frame, with the *x*-axis parallel to the shear direction, the *y*-axis normal to the shear plane, and the *z*-axis perpendicular to both the shear direction and the normal to the shear plane. All of these datasets are so far unpresented in the literature with the exception of 13 SZP samples previously described by Hansen and Warren (2015), which were collected following the same methodology. Microstructures from earlier datasets for SZP (Warren et al., 2008) and SZG (Skemer et al., 2010) are not included in the quantitative analysis here as they were collected using older generation EBSD systems and lack the data density necessary for examining subgrain structure.

The olivine CPOs in samples from SZA are analyzed for the first time in this study (Figure 3). As seen previously in the Fresno Bench shear zones (Skemer et al., 2010; Warren et al., 2008), SZA has a pre-existing CPO in the sample with zero shear strain, JP10-M15. As strain increases, the average [100]-axis orientation rotates from a maximum angle of 53˚ from the shear plane to an angle of 14˚ past the shear plane. The rotation is about the *z*-axis (perpendicular to both the shear direction and the shear plane normal), which is consistent with operation of slip systems with [100]

Burgers vectors (i.e., slip in the [100] direction). In SZP and SZG, the average [100]-axis orientation also rotates about the z-axis to align subparallel to the shear plain at high strain, but the rotation of the [100] axes in SZG (Skemer et al., 2010) evolves in the opposite direction from SZA and SZP (Figure S2).

At very low strain (<0.5) in SZA (JP10-M13 and JP10-M14), dual maxima are observed in the [100] axes (Figure 3). The first maximum is similar to the [100] maximum in the lowest strain sample (JP10-M15), aligned ~40˚ from the shear direction. The second maximum is aligned perpendicular to the first maximum, ~130˚ from the shear direction. The dual maxima in the [100] axes at very low strain in SZA is strikingly similar to that observed in SZP, in samples 3923-J06 and 3923-J08 (Figure 4). Similar features have also been observed in direct shear experiments, in which they were interpreted as potentially representing multiple slip directions (Zhang et al., 2000; Zhang & Karato, 1995). In that case, the disappearance of the second maximum at higher strain may represent recrystallization processes favoring crystals that are better oriented for [100]-slip.

At mid-to-high strains (≥3), the average [100]-axis orientation of each SZA sample is rotated by 6˚ to 14˚ past the shear plane, i.e., on the opposite side of the shear plane from the long axis of the finite strain ellipsoid (Figure 3). This relationship between the average [100]-axis orientation and the shear direction is also observed in two high-strain dunite samples from SZP (3924-J09b and 3924-J07; Figure S1) as well as all of the high strain samples from SZG (Figure 5). This behavior has been reported in experiments that produced an E-type CPO in olivine (Katayama et al., 2004). However, the antithetic orientation of the [100] axes usually arises by counter-clockwise rotation of the [100] maximum with progressive strain, as seen in SZG (Figure S2) and typically associated with deformation under wet conditions (see compilation by Skemer & Hansen, 2016). In contrast, the [100] maximum in SZA undergoes clockwise rotation (Figure S2). Clockwise rotation of the [100] maximum is a well documented phenomenon under dry conditions (again, see compilation by Skemer & Hansen, 2016), but there is no previously documented case in which [100] rotates past the shear plane. Thus, the CPO evolution in SZA is unique compared to other naturally and experimentally deformed samples.

The evolution of the [010] and [001] axes in SZA is far less systematic than that of the [100] axes (Figure 3). Both sets of axes oscillate between having their average orientations closer to the *y*-axis (shear plane normal) or to the *z*-axis of the pole figures. These fluctuations in the average orientation of the [010] and [001] axes are not regular, nor are they clearly a function of strain. SZP and SZG also exhibit a complicated evolution of these axes (Figures 4 and 5).

The [010] and [001] axes are at least marginally girdled in samples from all three shear zones. Examining the shape parameter K for each axis, where $0<K<1$ represents a girdled texture and $K>1$ represents a point maximum (Woodcock, 1977), nearly every sample exhibits girdled [010] axes (Figure 6b). Many samples also exhibit girdled [001] axes (Figure 6c). In contrast, the [100] axes are almost all point maxima (Figure 6a).

The olivine CPOs in samples from the Fresno Bench shear zones (Figures 3–5) can be qualitatively categorized as A-type or E-type depending on the average orientation of the three axes of olivine compared to the theoretical CPO (Figure 1). Since both CPO types are associated with slip systems with [100] Burgers vectors, the classification of A-type and E-type CPOs is dependent on the behavior of the [010] and [001] axes. In A-type CPOs, the [010] axes are subparallel to the pole to the shear plane and the [001] axes are subparallel to the *z*-axis of the pole figure. In E-type CPOs, on the other hand, this is reversed. The [010] axes are subparallel to the *z*-axis, and the [001] axes are subparallel to the pole to the shear plane. However, in many of the samples presented here, CPO classification can be ambiguous as the olivine textures are often relatively girdled in the [010] and [001] axes (Figure 6b, 6c). In addition, some textures exhibit average [010]- and [001]-axis orientations that are intermediate between the expected orientations for A-type and E-type (Figure 3–5). Of the CPOs examined in this study (including the duplicate samples 3925-G02-f and JP10-M08-KK), we classify 8 as A-type, 10 as E-type, and 12 as ambiguous (Table 1). All samples that could be classified as the "D-type" CPO, for which the [100] axes are point maxima and the [010] and [001] axes are girdled (Jung and Karato, 2001; Jung et al., 2006), are included in the ambiguous category.

Overall, samples from SZA exhibit moderate to strong textures, with the J-index ranging from 1.7 to 4.9 (Table S1) and the M-index (Skemer et al., 2005) ranging from 0.03 to 0.14 (Table 1). Similar ranges for these two parameters have also been observed in SZP and SZG (Hansen & Warren, 2015; Skemer et al., 2010; Warren et al., 2008). In all three shear zones, the texture strength does not increase systematically with increasing strain (Figure 6f).

4.2. Low-angle misorientation analysis

The A-type and E-type CPOs measured in SZA, SZP, and SZG are traditionally interpreted as representing the activation of different slip systems: [100](010) for A-type and [100](001) for E-type (Jung et al., 2006; Karato et al., 2008; Skemer et al., 2012). We examined the rotation axes of low-angle misorientations (1–10°) to help corroborate the slip system activity inferred from the CPOs. The orientations of these low-angle misorientation axes are plotted in the crystal reference frame in Figure 3–5. In this analysis, we assume that the low-angle misorientations are associated with tilt walls composed of edge dislocations of the major slip systems of olivine. If, on the one hand, tilt walls are composed of predominantly [100](010) dislocations, the misorientation axis should be parallel to the [001] (e.g., Lloyd et al., 1997). If, on the other hand, the tilt walls are composed of predominantly [100](001) dislocations, the misorientation axis should be parallel to [010]. Tilt walls composed of combinations of [100](010) and [100](001) dislocations will have misorientation axes at intermediate orientations between [010] and [001].

In every MIPF (Figure 3–5), a peak is present in the misorientation axis distribution near [010], which is consistent with slip on the [100](001) system. Additional clusters of misorientation axes also occur between [010] and [001] in most samples, consistent with the activation of multiple slip systems with [100] Burgers vectors.

One of the highest strain SZA samples, JP10-M08, is particularly notable in the agreement observed between the CPO and the low-angle misorientations in terms of slip system activation (Figure 3). The average orientations of the olivine axes are indicative of an E-type CPO, or slip on the [100](001) system. This matches the most common misorientation axis of [010] seen in the MIPF for that sample. The slight girdling of the [010] and [001] axes, representative of some proportion of activity on the [100](010) slip system, is matched by a smaller proportion of misorientation axes intermediate between the [010] and [001] axes. However, most samples do not exhibit strong agreement between the slip system inferred from the CPO and the slip system inferred from low-angle misorientation axes.

4.3. Piezometry

The differential stress during viscous deformation in the mantle is often assessed using a grain size or subgrain-size piezometer, based on the grain size reduction that is driven by dynamic recrystallization in response to applied stresses (e.g., Drury, 2005; Mercier et al., 1977; Twiss, 1977; Zeuch & Green, 1984). Using the olivine grain-size piezometer (e.g., Karato et al., 1980; Van der Wal et al., 1993), the average grain size range of 610 µm down to 180 µm in the shear zones yields differential stresses of 9 MPa up to 25 MPa, respectively (Table S1). The stresses recorded by the grain-size piezometer do not vary systematically as a function of strain in any of the shear zones, except for the high-strain samples from SZA and from SZG, which have smaller grain sizes than the other samples (Figure 6d).

However, the olivine grain-size piezometer (Karato et al., 1980; Van der Wal et al., 1993) was developed for monophase aggregates of olivine, whereas the samples from these shear zones are predominantly harzburgite. Since the presence of a second phase can result in smaller grain sizes than expected for a given stress due to processes such as grain-boundary pinning (e.g., Tasaka et al., 2017; Warren & Hirth, 2006), we also utilize a subgrain-size piezometer to quantify differential stress, which should be unaffected by the presence of another phase. Based on the detailed assessment of subgrain-size piezometers in Hansen and Warren (2015), the subgrain size piezometer of Toriumi (1979) is the most applicable to the shear zone samples in this study. The average subgrain sizes of 250 µm down to 95 µm yield stresses from 5 MPa up to 14 MPa using this piezometer (Table 1). In SZP, Hansen and Warren (2015) observed that stresses recorded by the subgrain-size piezometer are relatively constant as a function of strain, although the dunites record higher stresses than the harzburgites. In both SZA and SZG, however, the stresses recorded by the subgrain-size piezometer increase toward the center of the shear zone (Figure 6e).

4.4. Constraining shear-zone water contents

To evaluate the relationship between water in nominally anhydrous minerals and microstructures, we used secondary ion mass spectrometry to examine water concentrations in orthopyroxene from 18 samples: 9 from SZA, 7 from SZP, and 2 from SZG. Details of the analyses are described in a companion study that explores the systematics of geochemical variation across the shear zones (Kumamoto et al., in revision). Here we focus on the information relevant to understanding the relationship between water and CPO. Concentrations across the shear zones are variable, ranging from 180 to 334 ppm H_2O (Table 1). Variation within a sample, averaged over 2–6 grains with multiple points per grain, was on the order of $1\sigma = 18$ ppm, smaller than the measured inter-sample variations.

Water concentrations were also measured in olivine in 10 Fresno Bench samples, and these have an average of 9 ± 3 ppm across all three shear zones (Kumamoto et al., in revision). Differences among the shear zones are not resolvable within the precision of the current data set. These low water concentrations in olivine are similar to observations in other peridotites (2.0–5.0 ppm H_2O at mid-ocean ridges; Peslier, 2010; Warren & Hauri, 2014), where they have been interpreted as representing degassing prior to emplacement. Therefore, we also calculated olivine water concentrations that would have been in equilibrium with orthopyroxene, using the average experimentally-determined partition coefficient $D^{ol/opx}$ of 0.11 (Aubaud et al., 2004; Hauri et al., 2006; Tenner et al., 2009). We have not applied a partition coefficient as a function of pressure, temperature, or composition (e.g., the temperature dependence described by Grant et al., 2006; or the aluminum dependence described in O'Leary et al., 2010 for clinopyroxene) as the 12 available experimental values for aluminum-bearing systems (Aubaud et al., 2004; Hauri et al., 2006) do not provide enough data to parameterize these dependencies. Olivine water concentrations based on this partition coefficient range from 20 ppm H_2O (317 ppm H/Si) to 37 ppm H_2O (588 ppm H/Si).

Measured olivine water contents are all lower than water concentrations calculated from orthopyroxene concentrations. The mismatch between olivine and orthopyroxene could represent either the dehydration of olivine, the rehydration of orthopyroxene by later events, or some combination of dehydration and rehydration of one or both phases (e.g., Warren & Hauri, 2014). However, the systematic behavior of transects measuring water in orthopyroxene across all three shear zones suggests that the water concentrations in orthopyroxene reflect high-temperature processes associated with melt transport and shear-zone formation (Kumamoto et al., in revision). Even if dehydration or rehydration of the orthopyroxene has occurred, the relative variations in the water contents preserved in orthopyroxene can be taken as representative of the relative variations in water content during shear zone formation (Kumamoto et al., in revision).

5. Discussion

Olivine CPOs in the Fresno Bench shear zones suggest that slip systems with [100] Burgers vectors were the most active slip systems during deformation, as evidenced by the rotation of the [100] axes towards the shear direction with increasing strain. Slip on [100](010) is often referred to as "easy slip" due to the low strength of that slip system in olivine (e.g., Durham & Goetze, 1977) and its apparent prevalence in mantle samples (e.g., Tommasi et al., 2000). Experiments have indicated that [100](001) slip is almost as weak as [100](010) slip under dry conditions (Bai et al., 1991), and these two slip systems are often given equal strengths in textural evolution models (e.g., Tommasi et al., 2000).

Based on girdling in the [010]- and [001]-axis orientations (Figures 3–5), both [100](010) and [100](001) were active in most samples during deformation in the Fresno Bench shear zones. This interpretation is similar to that of Hansen et al. (2014), who previously interpreted girdled D-type textures in experimental samples as representing competition between the [100](010) and [100](001) slip systems. The low-angle misorientation distributions (Figures 3–5) in olivine for our samples corroborate this hypothesis, with even high strain samples exhibiting low-angle misorientation axes varying between [010] and [001]. However, A-type and E-type CPOs are not always associated with the expected misorientation distribution. In addition, the CPO type does not directly correlate with the magnitude of the finite shear strain; instead, the CPO type oscillates between A-type, E-type, and ambiguous with increasing strain. To explain the olivine CPO variability in the Fresno Bench shear zones, we explore three factors: variations in water abundance, the presence of a pre-existing CPO, and the effect of deformation kinematics.

5.1. The influence of water

Experimental studies have suggested that the dominant slip system in olivine can change as a function of differential stress and water content, leading to different CPOs (Jung et al., 2006; Jung & Karato, 2001; Katayama et al., 2004), as illustrated in Figure 7a. For our shear-zone samples, a transition between the A-type CPO (drier conditions) and the E-type CPO (wetter conditions) is expected at a concentration of ~800 ppm H/Si in olivine, given our estimates for differential stress during deformation. Previous work in the Josephine Peridotite suggested that a difference in water concentration between shear zones may explain the different CPOs observed at high strains in the Fresno Bench shear zones (Skemer et al., 2010, 2013). This conclusion was based on the observation that the center of SZG (3925-G01) has an E-type CPO and a higher water content, while the center of SZP (3924-J08) has a CPO more similar to A-type and a lower water content.

Our detailed transects of water content across the shear zones (Kumamoto et al., in revision) reveal much more complex variations in water abundances than suggested by Skemer et al. (2013). Kumamoto et al. (in revision) suggest that the water concentrations measured in the Fresno Bench orthopyroxenes reflect high-temperature processes associated with melt transport and deformation. However, the observed variations do not correlate with CPO type (Figure 7), implying that the relationship between water and CPO is not straightforward. Water concentrations from direct measurements of olivine, as well as calculations of olivine water contents from measurements in orthopyroxene, are all much lower than the boundary between A-type and E-type suggested by Jung et al. (2006) and related studies (Figure 7). Importantly, samples with A-type CPOs have similar water concentrations to samples with E-type CPOs.

One possibility for the discrepancies between our naturally deformed samples and the experimentally deformed samples (Jung et al., 2006; Jung & Karato, 2001; Katayama et al., 2004) may be differences in the deformation conditions. Experiments were performed at differential stresses >100 MPa and strain rates of $\sim 10^{-5}$ s^{-1} (Jung et al., 2006). In contrast, the estimated differential stresses in the Fresno Bench shear zones, based on subgrain-size piezometry, are <20 MPa (Table 1), well below the range of stresses measured in experiments. Strain rates are estimated to be $\sim 10^{-12}$–10^{-14} s^{-1}, based on olivine deformation by grain boundary sliding or wet dislocation creep, the mechanisms suggested to be active in the shear zones (Hansen & Warren, 2015; Nevitt et al., 2019). Thus, extrapolating the experimentally-defined boundary between A-type and E-type linearly from the high stresses of the experiments to the comparatively low stresses observed in the Fresno Bench shear zones may not be appropriate. Instead, our data could be an indication that the boundary between A-type and E-type textures is diffuse at low stresses, and thus the observed CPO depends more on other factors.

Bernard and Behr (2017) suggested that the magnitude of strain, rather than the concentration of water, controls the principal slip plane in olivine. In their mantle xenolith suite, coarser-grained protogranular samples were more likely to have A-type CPOs, while porphyroclastic (i.e., slightly deformed) and mylonitic samples more often exhibited E-type CPOs. This broadly agrees with data from the Fresno Bench shear zones, in that the highest strain Josephine samples (strain ≥ 20) have olivine CPOs most similar to E-type. However, our dataset also contains many lower-strain samples with significant activation of the [100](001) slip system, evident in both the CPOs and the misorientation axis distributions for olivine (Figures 3–5). Therefore, other variables must be affecting the observed changes in CPO.

5.2. The influence of a pre-existing CPO

A key attribute of the naturally deformed Josephine samples is the presence of a CPO prior to shear-zone deformation. Most olivine deformation experiments that have been done to characterize CPO types were based on initially random textures, but experiments have also shown that the presence of a pre-existing CPO has a strong effect on microstructural evolution (e.g., Boneh & Skemer, 2014; Hansen et al., 2012; Hansen, Warren, et al., 2016). Samples from outside the Fresno Bench shear zones all have relatively strong textures, with an M-index of ~0.1, whereas an initially random texture has an M-index of 0. We hypothesize that differences in the initial CPO should affect CPO evolution in the Fresno Bench shear zones.

To investigate the role of a pre-existing CPO, we used the director-based textural evolution model developed by Hansen, Conrad, et al. (2016). In this model, the responses of each grain to an imposed velocity-gradient tensor are individually modeled, tracking the orientation of each crystallographic axis as a function of strain. The relative rotation rates associated with each slip system were calibrated using experimental results from Hansen et al. (2014) and Hansen, Warren, et al. (2016). These experiments on dry olivine were conducted in extension and torsion with and without pre-existing textures. To reasonably reproduce the CPOs observed in the experiments, the [100](010) and [100](001) slip-system rotation rates are set to nearly equal (Hansen, Conrad, et al., 2016), similar to other modeling studies that have used equal critical resolved shear stresses for those two slip systems to reproduce natural and experimental CPOs (e.g., Tommasi et al., 1999). The other two slip systems implemented in the calculation, [001](010) and [001](100), are assigned slip-system rotation rates that are slower by nearly an order of magnitude or more.

As a textural evolution model is not available for hydrous olivine, we use the relative slip-system rotation rates calibrated by Hansen, Conrad, et al. (2016) for dry olivine. Single-crystal experiments on olivine suggest that water unequally affects the strength of different slip systems and should thus affect their relative contributions to grain rotation (e.g., Karato, 1989; Mackwell et al., 1985), but the magnitude by which the strength of each slip system changes is not well constrained. In addition, since water concentrations are quite variable across the shear zones, the relative strengths of the slip systems will vary from sample to sample, further complicating attempts to more precisely model textural evolution in the shear zones. Hence, application of the textural evolution model at dry conditions provides a baseline test of the influence of a pre-existing CPO, against which future models can be tested.

Figure 8 depicts three simulations of olivine CPO evolution as a function of shear strain. The textural evolution model was run based on simple-shear kinematics with three different initial CPOs: a modeled random texture with 500 grains (Figure 8A), a low strain sample from SZP (3923-J06, Figure 8B), and the lowest strain SZA sample (JP10-M15, Figure 8C). The natural starting CPOs were chosen as they result from relatively low strain but allow us to observe how slight differences in the starting CPOs can affect CPO evolution.

In all three simulations, texture strength increases with increasing shear strain, similar to experimental observations (e.g., Hansen et al., 2014; Hansen, Warren, et al., 2016). This is counter to our natural samples, which do not show strong correlations between texture strength and shear strain (Figure 6; Skemer et al., 2010; Warren et al., 2008). Olivine CPOs from other peridotite localities (e.g., Ben Ismaïl & Mainprice, 1998; Bernard et al., 2019) also exhibit similar texture strengths to our samples, though strain is unquantified in these examples. The overprediction of texture strength by the Hansen, Conrad et al. (2016) model is observed in other texture models (e.g., VPSC in Signorelli & Tommasi, 2015). The differences between natural samples and experimental samples in this regard remains unclear but may reflect the multiphase lithology of the natural samples.

The model broadly reproduces the observed behavior of the [100] axes in the shear zones. Strong [100]-axis orientations are developed at a shear strain < 4, and this average [100]-axis maximum quickly rotates to become subparallel to the shear direction. Although this rotation occurs more rapidly in the models than in the natural samples, the high-strain [100]-axis orientations are similar to those observed in the shear zones.

The [010] and [001] axes also evolve rapidly in the simulations compared to the natural samples, reaching steady-state orientations representative of an A-type texture at a strain of ~4 (Figure 8). Prior to reaching steady-state, however, the evolution of the [010] and [001] axes exhibit variability from simulation to simulation. With JP10-M15 as the pre-existing texture, the [010] axes start subparallel to the *z*-axis and slowly become slightly girdled toward the *y*-axis (Figure 8).

The [001] axes have the opposite behavior, with the average orientation beginning subparallel to the *y*-axis and slowly becoming more girdled towards the *z*-axis.

Using 3923-J06 as the pre-existing texture, we observe more complicated behavior (Figure 8). 3923-J06 has dual maxima in both the [100] and the [001] axes (Figure 4). As strain increases, orientations more favorable for slip systems with [100] Burgers vectors begin to dominate the orientation distribution, and the second maximum, initially oriented perpendicular to the first maximum, disappears. Only one of the [100]-maxima and one of the [001]-maxima persist beyond a strain of 1. Interestingly, the maxima that persist are better oriented for [100](001) slip. However, with increasing strain, girdles develop in the [010]- and [001]-axis orientations, and by a strain of 6, an A-type texture dominates the CPO.

These results indicate that the presence of a pre-existing CPO can have a strong effect on CPO evolution at strains < 5, most notably in the behavior of the [010] and [001] axes. At higher strains, however, a pre-existing texture does not explain the protracted evolution of the [010] and [001] axes in the Fresno Bench shear zones, particularly the E-type CPOs in the highest-strain samples.

5.3. The influence of kinematics

Thus far, we have assumed that the Fresno Bench shear zones deformed in simple shear, an idealized framework often used for evaluating shear zone deformation (e.g., Davis, 1983; Herren, 1987; Ramsay, 1980; Skemer et al., 2010). However, recent studies on natural mantle rocks (Bernard et al., 2019; Chatzaras et al., 2016) have suggested that strain geometry, rather than stress or water content, may control a large range of olivine CPO observations. Additionally, studies of crustal shear zones have often identified more complex kinematics in areas where sufficient strain markers are available (e.g., De Paola et al., 2008; Nevitt et al., 2014).

With only a single strain marker (the deflection of the pyroxene foliation), the contribution of pure shear to the development of the Fresno Bench shear zones is unconstrained, but we can still evaluate how different kinematics may have affected CPO evolution in these samples using modeling techniques. For instance, Tommasi et al. (1999) used a viscoplastic self-consistent model to explore the role of deformation kinematics on the evolution of olivine CPOs up to equivalent strains of 1. In their models, simple shear combined with a component of pure shear, corresponding to extension in the y direction and compression in the z direction, produces a [010]-axis maximum parallel to the z-axis, equivalent to an E-type CPO.

We used the director-based textural evolution model from Hansen, Conrad, et al. (2016) with JP10-M15 (SZA initial texture) as the starting texture and the same slip-system rotation rates as implemented in Section 5.2 and Figure 8. The relative contribution of pure shear relative to simple shear was tested at 1% and 15%, producing the textural evolutions presented in Figure 9. In each series, pure shear is defined as equal extension in x (ε_{xx}) and y (ε_{yy}) plus shortening in z (ε_{zz}) to maintain constant volume. The shear strain (ε_{xy}) measured by foliation deflection is unchanged by the pure shear component as $\varepsilon_{xx} = \varepsilon_{yy}$. Hence, samples can be directly compared to the model outputs at the same shear strains.

The simulations presented in Figure 9 approximately reproduce several key characteristics of the natural shear-zone evolution in Figures 3–5. First, the [010] and [001] axes remain girdled up to high strains. The dominance of axis orientations representative of [100](010) slip vs [100](001) slip is a function of the magnitude of pure shear relative to simple shear. When pure shear is a very small component of the deformation (e.g., Figure 9A), the A-type texture ultimately dominates at high strain, as expected for simple shear. However, when a pure shear component is included such that $\varepsilon_{xx} = \varepsilon_{yy} = -0.5\varepsilon_{zz} = 15\%\ \varepsilon_{xy}$ (Figure 9B), the high-strain texture is more representative of the E-type CPO.

Another feature of the model outcomes is that at high shear strain (>8), the average orientation of the [100] axes is rotated past the shear plane (Figure 9). This feature is present even when the pure shear component is only 1% of the magnitude of the simple shear component. The rotation of the [100]-axis maximum past the shear plane is consistent with the olivine CPOs observed in SZA (Figure 3) and SZG (Figure 5), as well as other natural and experimental observations of E-type CPOs (e.g., Bernard & Behr, 2017; Katayama et al., 2004; Mehl et al., 2003). The rotation of the [100]-axis maximum past the shear plane has previously been difficult to explain, and the predicted presence of this rotation with even a small proportion of pure shear is a promising aspect of the textural evolution simulations. However, at these strains, the [010]- and [001] axes acquire some orientations in faint girdles that have not been observed in natural or experimental samples (Figure 9). The appearance of these orientations is possibly due to the exclusion of dynamic recrystallization in the model (cf. Signorelli & Tommasi, 2015). The complex girdling of these axis orientations at high strain suggests that this model requires further calibration and refinement, particularly for non-simple shear kinematics.

These simulations demonstrate that the texture variation we observe in the Fresno Bench shear zones can be explained by incorporating a component of pure shear in the deformation. Thus, the dominance of an A-type texture or E-type texture may depend more on the magnitude of the pure shear component relative to simple shear, as well as the magnitude of the finite shear strain, than on the water content.

5.4. Implications for interpreting seismic anisotropy

Understanding the controls on the formation and evolution of olivine CPO during mantle flow is critical for interpreting seismic anisotropy. However, observed patterns of seismic anisotropy do not always agree with models that predict CPO formation associated with mantle flow (e.g., Becker et al., 2014). In particular, the misfit between observed azimuthal anisotropy and the CPO model of Becker et al. (2008) is the highest in the vicinity of plate boundaries. Our evaluation of the Josephine shear zones provides insight on the mechanisms leading to either A-type or E-type CPOs. While these two CPO types do not produce different shear-wave splitting directions during subhorizontal shearing, they do result in different magnitudes of azimuthal and radial anisotropy (e.g., Becker et al., 2008). In addition, during vertical shearing, the A-type and E-type CPOs will produce markedly different shear-wave splitting directions.

Our results indicate that the transition between A-type and E-type CPOs can be dependent on both the pre-existing texture and deformation kinematics. These two factors are particularly pertinent at plate boundaries at which flow directions can vary over relatively small length scales and deformation can depart from simple shear. For instance, corner flow beneath mid-ocean ridges requires textures initially formed during upwelling to be subsequently overprinted by textures formed during horizontal shearing (e.g. Castelnau et al., 2009). As another example, at highly arcuate subduction zones, such as the Indonesian region (e.g. Di Leo et al., 2012), the complex tectonic arrangements could lead to deformation kinematics aside from simple shear. Thus, taking these factors into account may improve the agreement between observations of seismic anisotropy and predictions from geodynamic models.

6. Conclusions

A detailed investigation of three shear zones (SZA, SZG, and SZP) highlights the complex evolution of olivine CPO as a function of strain in ductile upper mantle shear zones in the Fresno Bench outcrop of the Josephine Peridotite. Microstructural analysis indicates that [100](010) and [100](001) are the dominant slip systems active in these samples, and that both slip systems are active in all samples. The relative dominance of one slip system over the other, previously suggested to be a function of water content, cannot be directly reconciled with the water concentrations present in these shear zones. Samples with A-type CPOs can have the same water contents as samples with E-type CPOs. Instead, we demonstrate that the presence of a texture prior to shear zone formation can have a large effect on the textural evolution at relatively low strains and can explain the E-type CPOs observed in the shear zones up to strains of ~2. In addition, incorporating pure shear in addition to simple shear can reproduce many details of the CPO evolution in the shear zones, including girdled [010] and [001] axes at low strain, the presence of an E-type CPO at high strain, and the tilt of the [100] axes past the shear plane at high strain in SZA. We suggest that a combination of a pre-existing CPO and kinematics departing from simple shear are the dominant controls on olivine CPO evolution in the Fresno Bench shear zones.

Acknowledgements

We thank Kendra Lynn for discussions on water in peridotite minerals and David Pollard for thoughtful and constructive comments on a draft of this manuscript. We also thank Martin Grove and Wendy Mao for their input on these results. Thanks also to Rachel Bernard and an anonymous reviewer for their constructive comments on this work. This material is based upon work supported by the National Science Foundation under Grants EAR-1255620 and EAR-1625032 to J.M.W. and EAR-1806791 to K.M.K. EBSD data are available from EarthChem Library at https://doi.org/10.1594/IEDA/111365.

Figure Captions

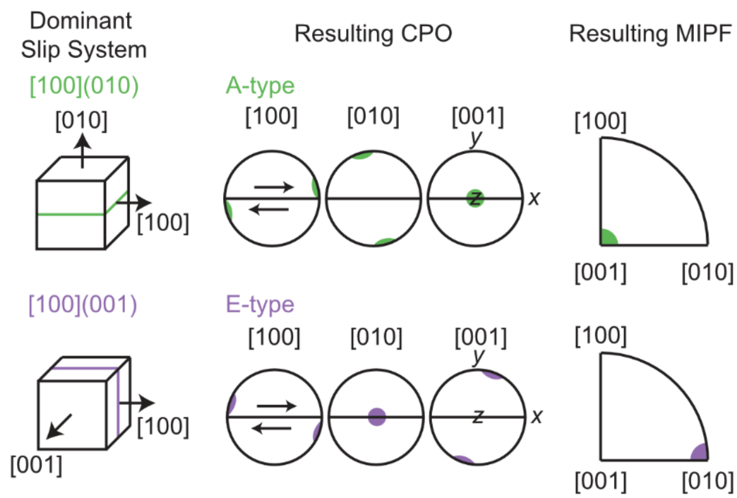

Figure 1. The two main slip systems observed in the Fresno Bench shear zones, along with the CPO and misorientation axis orientations expected from the activation of these slip system during simple shear. The colored lines in the dominant slip systems denote the relevant slip plane. The CPOs are a schematic representation of the expected average crystal orientations after deformation, with the horizontal line representing the shear plane. The coordinate system for the axes are labeled in the [001] pole figures and are the same for each pole figure. In this coordinate system, *x* is parallel to the shear direction, and *y* is the pole to the shear plane. The shear sense is right lateral. Schematic orientations of the expected low-angle misorientation axes are plotted in the misorientation-axis inverse pole figures (MIPFs). After Skemer et al. (2012).

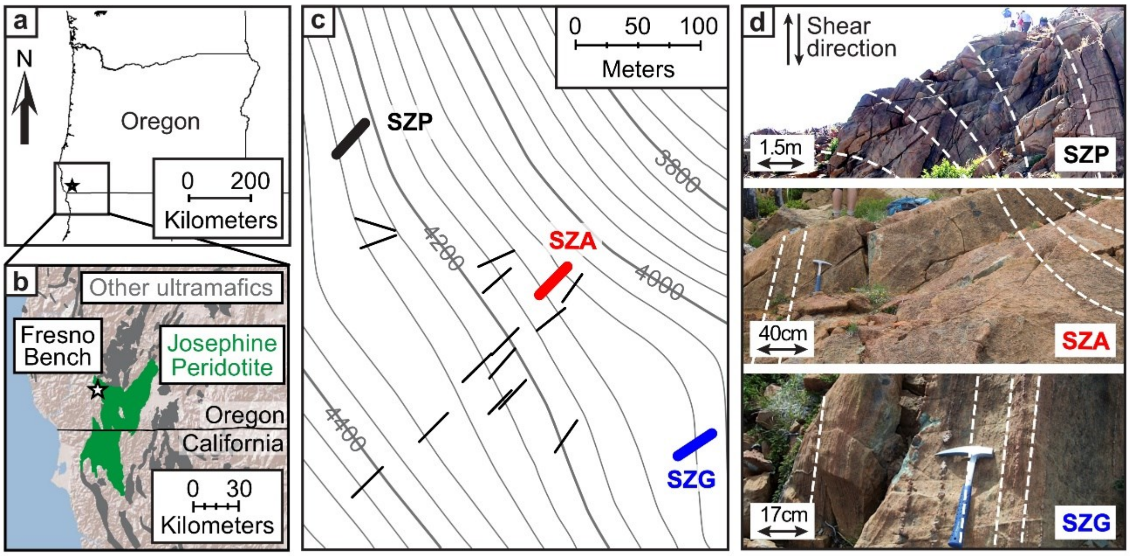

Figure 2: (**a**) The location of the Josephine Peridotite in Oregon. (**b**) The Fresno Bench outcrop (star) in the Josephine Peridotite (green). Other ultramafic units are in grey. Fresno Bench is located at 42°10'20"N, 123°58'53"W. After Skemer et al. (2013). (**c**) A map of the locations of shear zones on the Fresno Bench outcrop. The three analyzed shear zones are marked by bold lines, with the orientation indicating the strike of the shear plane. Thinner black lines represent the shear planes of other shear zones in the Fresno Bench outcrop. The same length line is used to indicate the location of each shear zone and does not indicate the size of the exposure. (**d**) Field photos of a portion of the three analyzed shear zones in the field. White dashed lines indicate the orientation of the pyroxene foliation.

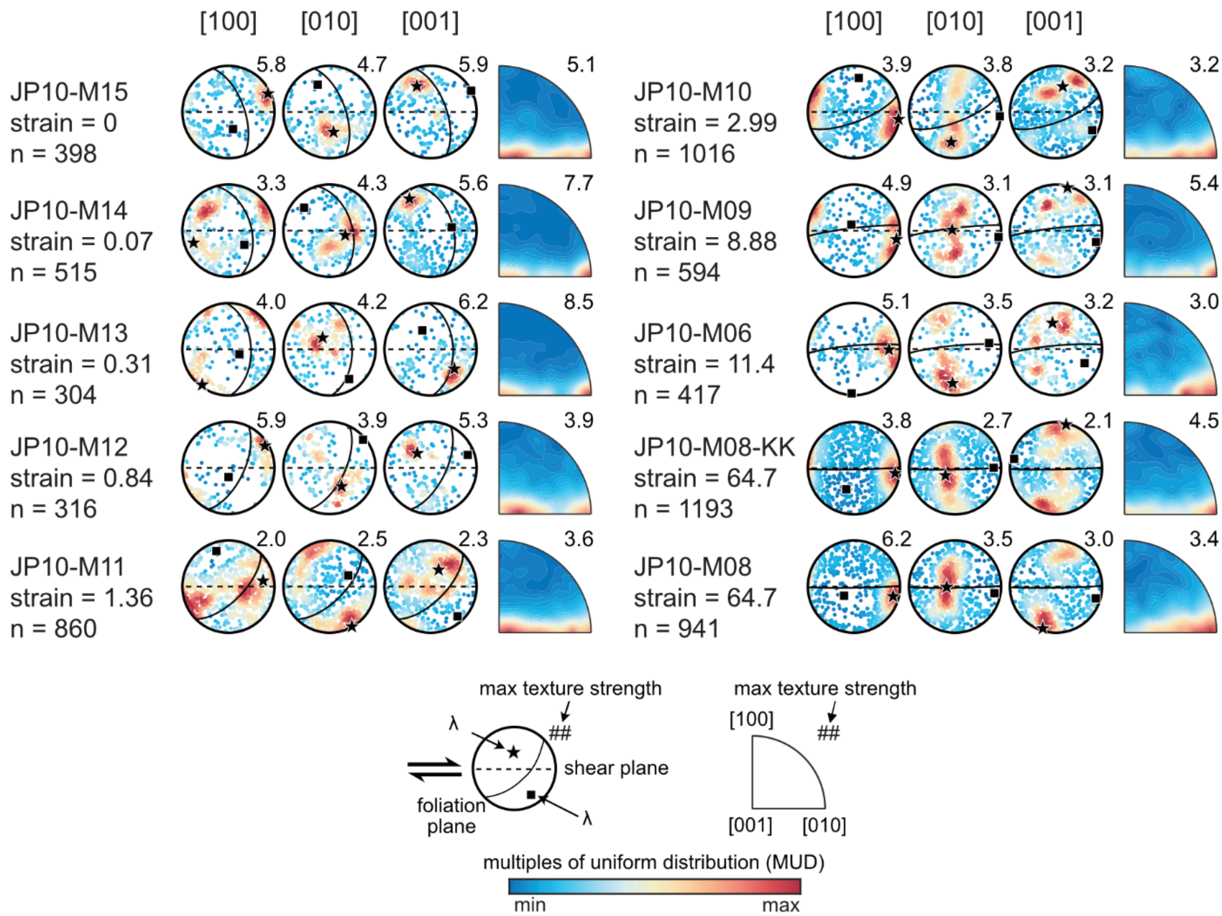

Figure 3. Pole figures of crystal orientations and inverse pole figures of low-angle misorientation axes for olivine in each sample in SZA organized as a function of strain. All pole figures are lower hemisphere, equal-area projections. The sense of shear is right-lateral. JP10-M08 and JP10-M08-KK are two sections from the same sample. For each CPO, individual points represent the average orientation of each grain, and they are colored by multiples of a uniform distribution (MUD). The maximum MUD for each axis is presented to the upper right of each pole figure. Stars represent λ_1, the average orientation of a crystallographic axis based on eigenvalue analysis (Woodcock, 1977). Squares represent λ_3, the pole to the plane that best fits all of the orientations of that axis. The foliation measured in the field for each sample is shown as a black great circle. The horizontal dashed line represents the shear plane. Inverse pole figures of low-angle misorientation axes are also colored by MUD.

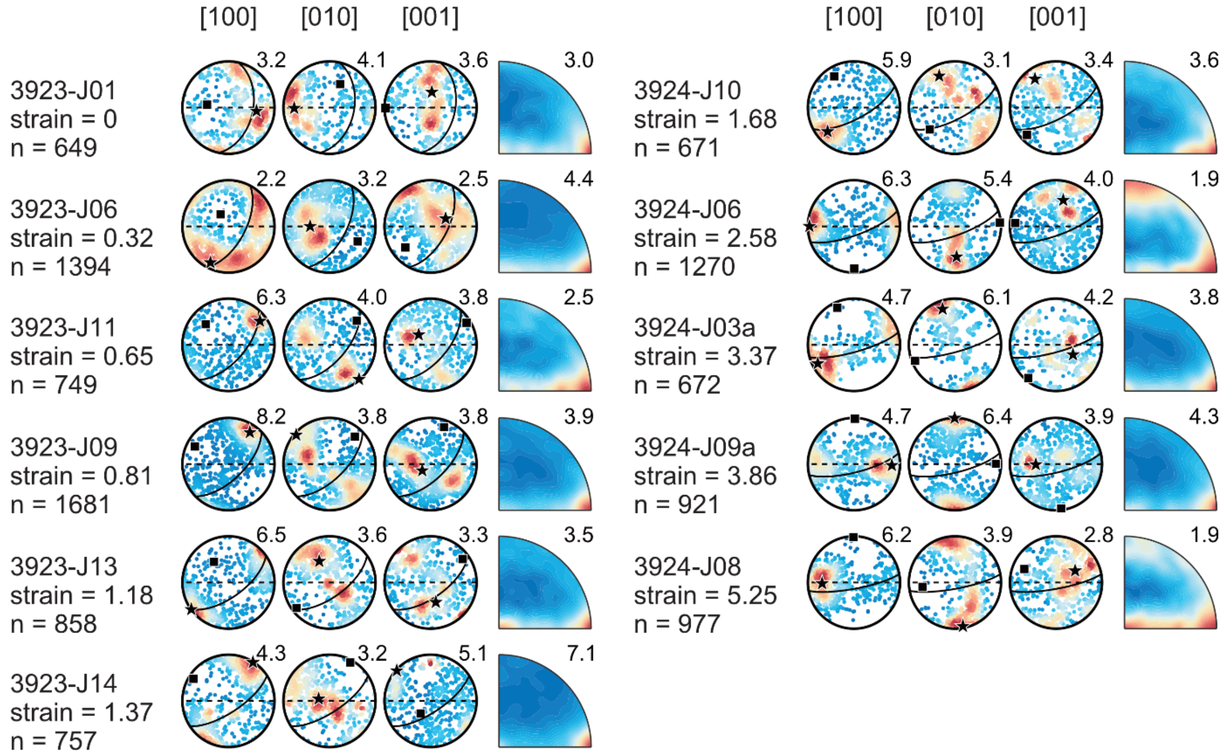

Figure 4. Pole figures of crystal orientations and inverse pole figures of low-angle misorientations for olivine in harzburgite samples from SZP organized as a function of strain. Data from this study and Hansen and Warren (2015). Annotations are the same as in Figure 3.

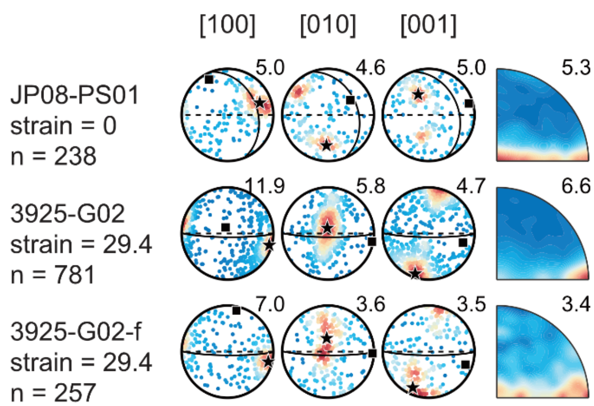

Figure 5. Pole figures of crystal orientations and inverse pole figures of low-angle misorientation axes for olivine in samples from SZG. 3925-G02-f is from the finer-grained portion of 3925-G02. Annotations are the same as in Figure 3.

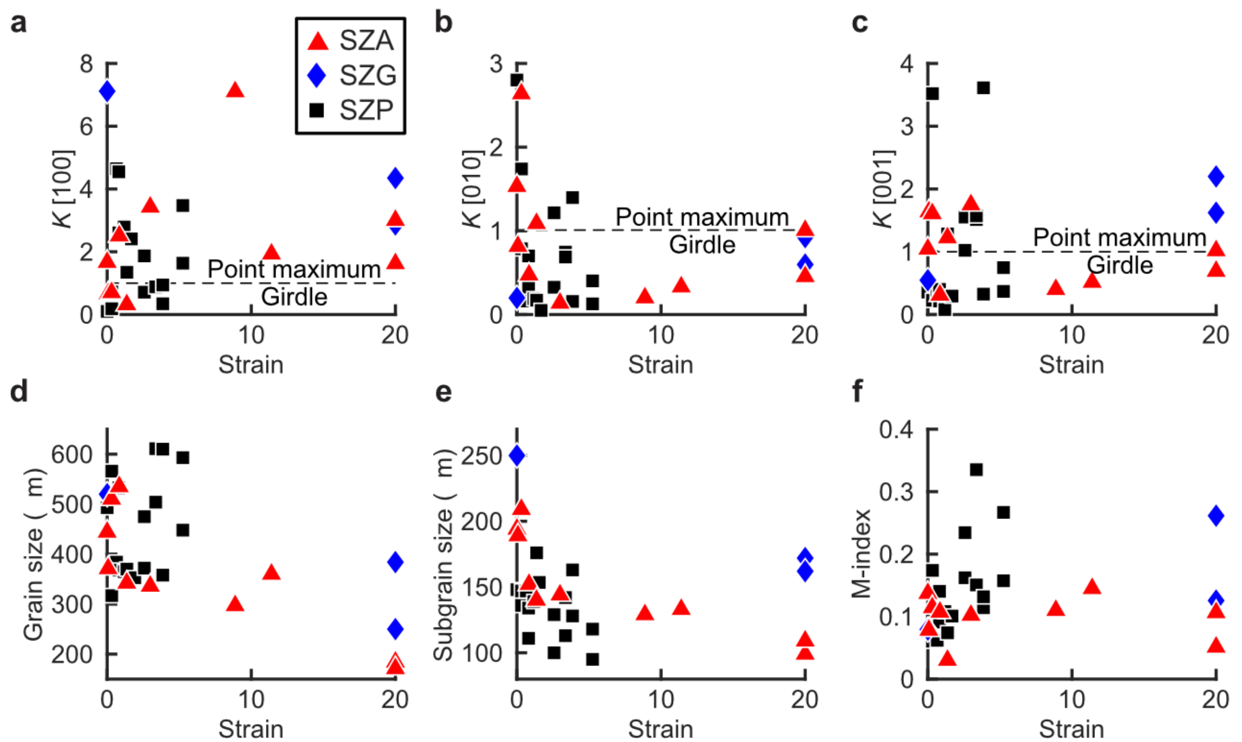

Figure 6. Microstructural variations as a function of strain in the Fresno Bench shear zones. Strain is capped at 20 in all plots. (**a–c**) The shape parameter, *K*, of each olivine axis as a function of strain. The dashed line indicates the boundary between point maxima (K>1) and girdled textures (K<1). (**d**) Grain size vs strain. Grain sizes are calculated using the linear-intercept method and reported with a geometric correction factor of 1.5. (**e**) Subgrain size vs strain. Subgrain sizes are also reported with a geometric correction factor of 1.5. (**f**) M-index vs strain.

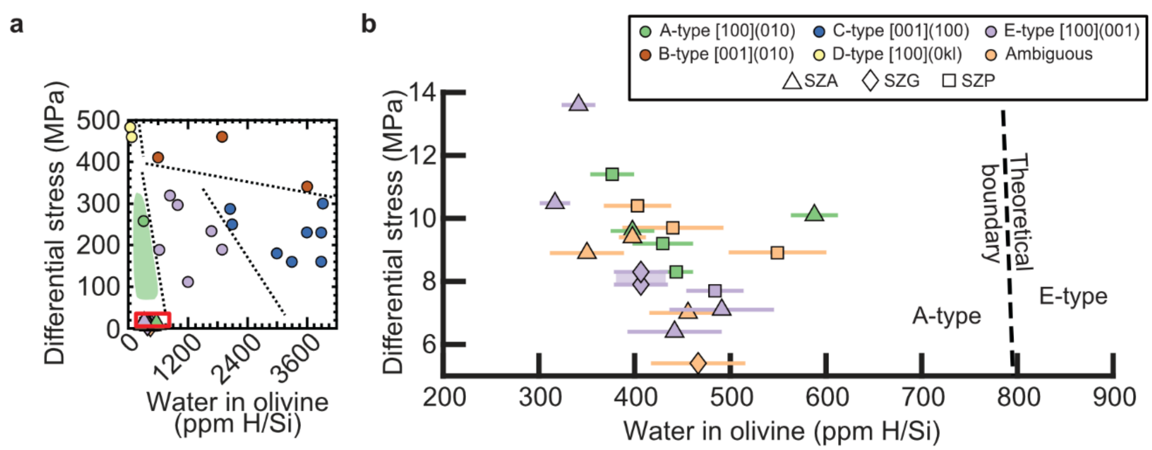

Figure 7. (**a**) CPO type and associated dominant slip system, as a function of water content and differential stress, after Jung et al. (2006). Circles are experiments from Jung et al. (2006), Jung and Karato (2001), and Katayama et al. (2004) and are colored by CPO type. The filled field represents the conditions of experiments from Zhang and Karato (1995) which produced A-type CPOs. Data from the Fresno Bench shear zones plot at low water and low stress relative to the experiments. Water concentrations from previous studies are multiplied by a factor of 3 to account for differences in data reduction between the Paterson (1982) calibration used by Jung and co-workers (Jung et al., 2006; Jung & Karato, 2001; Katayama et al., 2004) and the Bell et al. (2003) calibration that forms the basis of measurements of the Josephine samples (Kumamoto et al., in revision). (**b**) CPO data for samples from the Fresno Bench shear zones as a function of their water content and differential stress. The water content in olivine is calculated from the measured water content in orthopyroxene using an experimental mineral-mineral partition coefficient of 0.11 (Aubaud et al., 2004; Hauri et al., 2006; Tenner et al., 2009). Error bars on water contents are 1σ uncertainties. The dashed black line is the theoretical boundary between A-type and E-type CPOs from Jung et al. (2006). Some olivine CPOs from this study are classified as ambiguous, as they show significant girdling, dual maxima, or maxima intermediate between those associated with A-type and E-type textures.

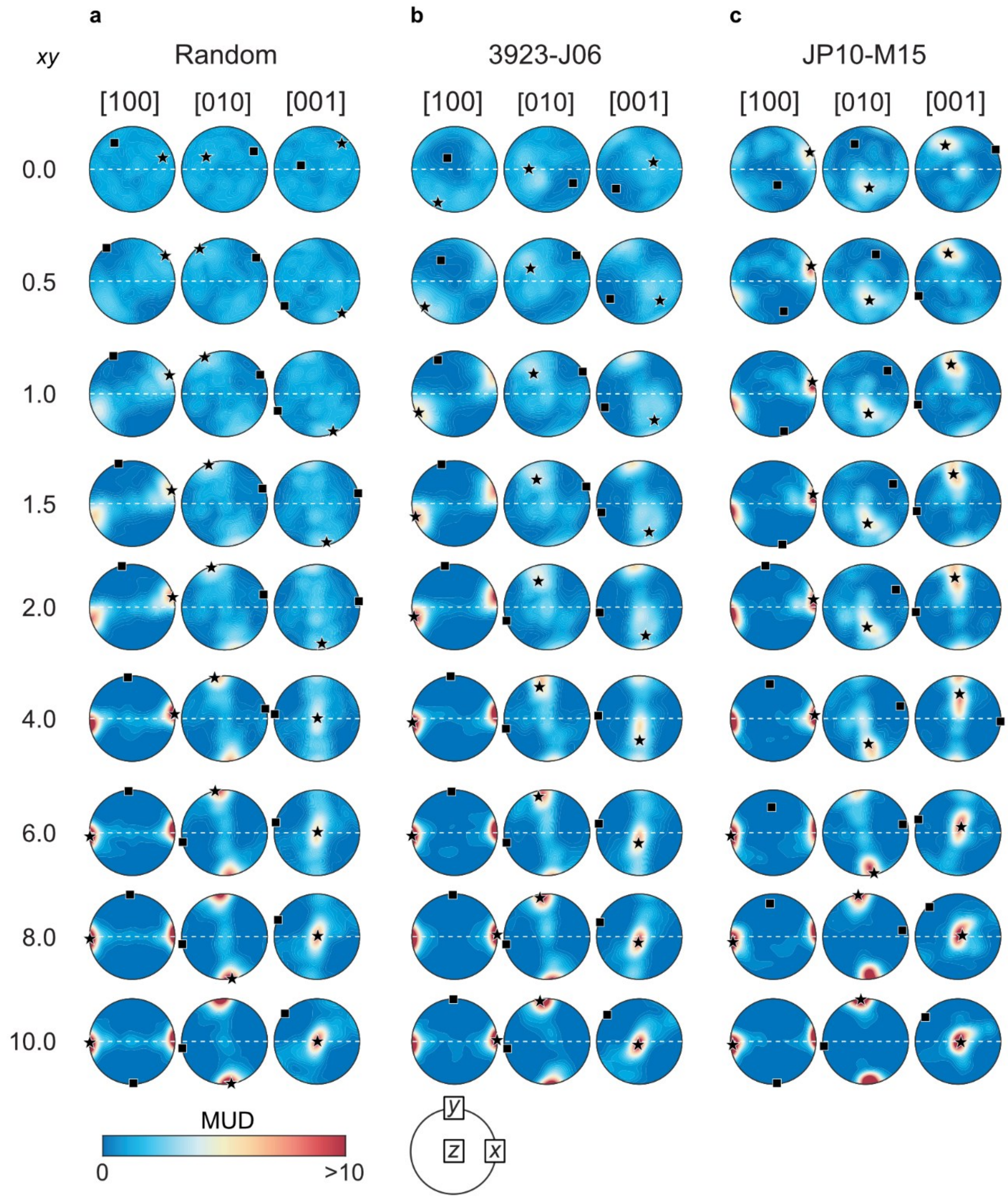

Figure 8. Results from the textural evolution model for olivine CPOs for three different initial textures. The starting CPOs are (**a**) a random texture, (**b**) the texture of 3923-J06, a low-strain sample from SZP, and (**c**) the texture of JP10-M15, a low-strain sample from SZA. The horizontal white dashed line represents the shear plane. Stars represent λ_1 and squares represent λ_3 (analysis following Woodcock, 1977), as in Figures 3–5. All pole figures are colored by MUD to a maximum of 10.

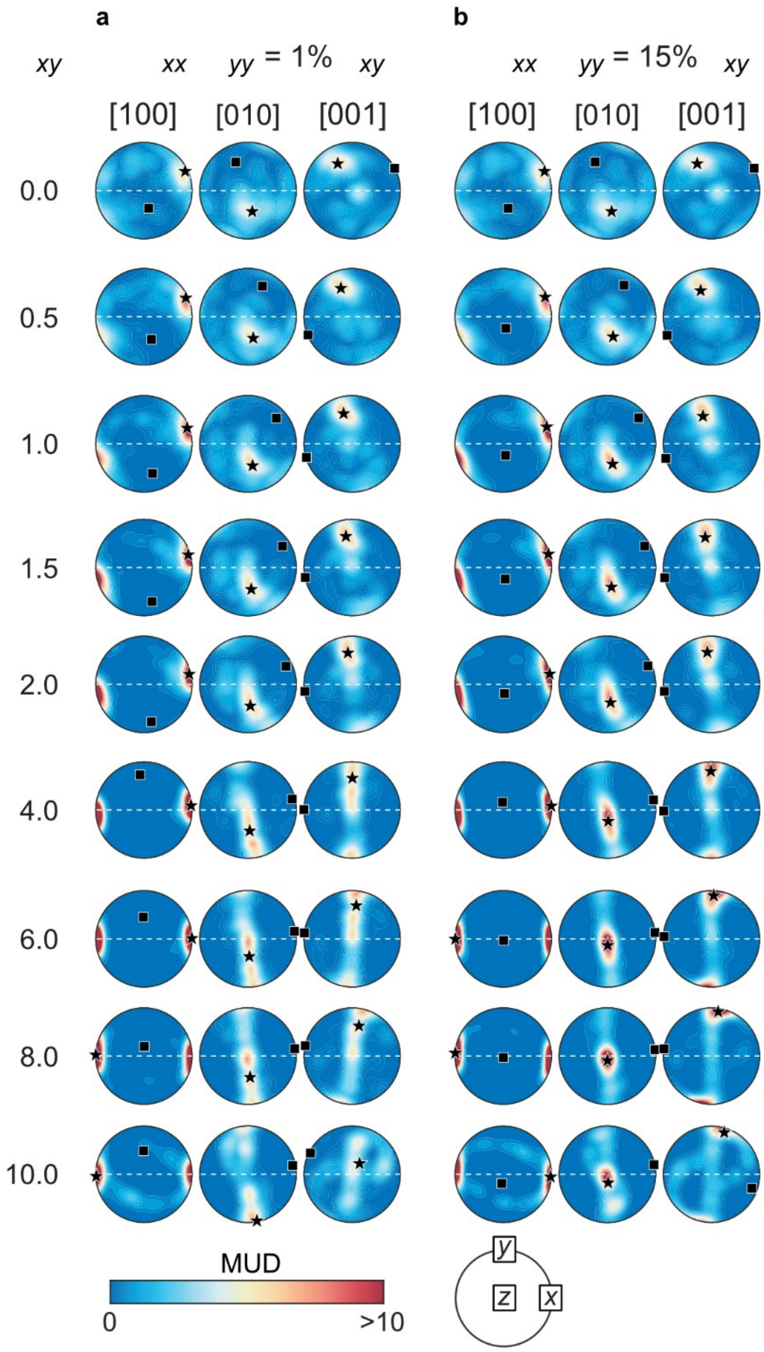

Figure 9. Results of textural evolution simulations in which different magnitudes of pure shear were added to simple shear, using JP10-M15 from SZA as the starting texture. The magnitude of pure shear is set to be a specific percentage of the simple shear: (**a**) $\varepsilon_{xx} = \varepsilon_{yy} = 1\%\ \varepsilon_{xy}$ and $\varepsilon_{zz} = -2\%\ \varepsilon_{xy}$ and (**b**) $\varepsilon_{xx} = \varepsilon_{yy} = 15\%\ \varepsilon_{xy}$ and $\varepsilon_{zz} = -30\%\ \varepsilon_{xy}$. The horizontal white dashed line represents the shear plane. Stars represent λ_1 and squares represent λ_3 (analysis following Woodcock, 1977), as in Figures 3–5. All pole figures are colored by MUD to a maximum of 10.

Table

Table 1. ***Microstructural Data for Each Sample in this Study***

	Lithology	Strain	Grain size (µm)	Subgrain size (µm)	Stress (MPa)	M-index	Opx H_2O (ppm)	Ol H_2O (ppm H/Si)	CPO type
SZA									
JP10-M15	Harz	0	444	194	7.0	0.14	259 ± 23	456 ± 40	ambiguous
JP10-M14	Harz	0.07	371	189	7.1	0.08	279 ± 31	491 ± 55	E-type
JP10-M13	Harz	0.31	510	209	6.4	0.11	251 ± 28	442 ± 49	E-type
JP10-M12	Harz	0.84	535	152	8.9	0.11	199 ± 22	350 ± 39	ambiguous
JP10-M11	Harz	1.36	342	140	9.6	0.03	226 ± 13	398 ± 23	A-type
JP10-M10	Harz	2.99	336	144	9.4	0.10	226 ± 8	398 ± 14	ambiguous
JP10-M09	Harz	8.88	297	129	10.5	0.11	180 ± 9	317 ± 16	E-type
JP10-M06	Harz	11.4	360	133	10.1	0.14	334 ± 14	588 ± 25	A-type
JP10-M08	Harz	20	184	99	13.6	0.11	194 ± 10	341 ± 18	E-type
JP10-M08-KK	Harz	20	171	109	12.3	0.05	194 ± 10	341 ± 18	E-type
SZG									
JP08-PS01	Harz	0	520	250	5.4	0.08	265 ± 28	466 ± 49	ambiguous
3925-G02	Harz	20	384	172	7.9	0.26	231 ± 16	407 ± 28	E-type
3925-G02-f	Harz	20	250	162	8.3	0.13	231 ± 16	407 ± 28	E-type
SZP									
3923-J01	Harz	0	493	148	9.1	0.08	---	---	ambiguous
3923-J06	Harz	0.32	317	147	9.2	0.06	---	---	ambiguous
3923-J07	Dun	0.32	566	136	9.9	0.17	---	---	ambiguous
3923-J11	Harz	0.65	384	147	9.2	0.06	244 ± 18	429 ± 32	A-type
3923-J08	Dun	0.81	368	111	12.1	0.09	---	---	A-type
3923-J09	Harz	0.81	533	134	10.0	0.14	---	---	A-type
3923-J13	Harz	1.18	365	139	9.7	0.11	250 ± 30	440 ± 53	ambiguous
3923-J14	Harz	1.37	370	176	7.7	0.07	275 ± 17	484 ± 30	E-type
3924-J10	Harz	1.68	348	152	8.9	0.10	312 ± 29	549 ± 51	ambiguous
3924-J05	Dun	2.58	475	100	13.5	0.23	---	---	ambiguous
3924-J06	Harz	2.58	372	129	10.4	0.16	229 ± 20	403 ± 35	ambiguous
3924-J03a	Harz	3.37	504	142	9.5	0.15	---	---	A-type
3924-J03b	Dun	3.37	611	113	12.0	0.34	---	---	E-type
3924-J09a	Harz	3.86	358	163	8.3	0.11	252 ± 10	444 ± 18	A-type
3924-J09b	Dun	3.86	610	128	10.5	0.13	---	---	ambiguous
3924-J07	Dun	5.25	593	95	14.2	0.27	---	---	E-type
3924-J08	Harz	5.25	448	118	11.4	0.16	214 ± 13	377 ± 23	A-type

Note. Stress is calculated based on subgrain size using the piezometer of Toriumi (1979). Water concentrations in olivine are calculated from orthopyroxene water concentrations (Kumamoto et al., in revision).

References

Aubaud, C., Hauri, E. H., & Hirschmann, M. M. (2004). Hydrogen partition coefficients between nominally anhydrous minerals and basaltic melts. *Geophysical Research Letters*, *31*(L20611). https://doi.org/10.1029/2004GL021341

Bachmann, F., Hielscher, R., & Schaeben, H. (2010). Texture Analysis with MTEX – Free and Open Source Software Toolbox. *Solid State Phenomena*, *160*, 63–68. https://doi.org/10.4028/www.scientific.net/SSP.160.63

Becker, T. W., Kustowski, B., & Ekström, G. (2008). Radial seismic anisotropy as a constraint for upper mantle rheology. *Earth and Planetary Science Letters*, *267*(1), 213–227. https://doi.org/10.1016/j.epsl.2007.11.038

Becker, T. W., Conrad, C. P., Schaeffer, A. J., & Lebedev, S. (2014). Origin of azimuthal seismic anisotropy in oceanic plates and mantle. *Earth and Planetary Science Letters*, *401*, 236–250. https://doi.org/10.1016/j.epsl.2014.06.014

Behr, W. M., & Hirth, G. (2014). Rheological properties of the mantle lid beneath the Mojave region in southern California. *Earth and Planetary Science Letters*, *393*, 60–72. https://doi.org/10.1016/j.epsl.2014.02.039

Bell, D. R., Rossman, G. R., Maldener, J., Endisch, D., & Rauch, F. (2003). Hydroxide in olivine: A quantitative determination of the absolute amount and calibration of the IR spectrum. *Journal of Geophysical Research*, *108*(B2), 672. https://doi.org/10.1029/2001JB000679

Ben Ismaïl, W., & Mainprice, D. (1998). An olivine fabric database: an overview of upper mantle fabrics and seismic anisotropy. *Tectonophysics*, *296*(1), 145–157. https://doi.org/10.1016/S0040-1951(98)00141-3

Bernard, R. E., & Behr, W. M. (2017). Fabric heterogeneity in the Mojave lower crust and lithospheric mantle in Southern California. *Journal of Geophysical Research: Solid Earth*, *122*(7), 5000–5025. https://doi.org/10.1002/2017JB014280

Bernard, R. E., Behr, W. M., Becker, T. W., & Young, D. J. (2019). Relationships between olivine CPO and deformation parameters in naturally deformed rocks and implications for mantle seismic anisotropy. *Geochemistry, Geophysics, Geosystems*, *20*. https://doi.org/10.1029/2019GC008289

Boneh, Y., & Skemer, P. (2014). The effect of deformation history on the evolution of olivine CPO. *Earth and Planetary Science Letters*, *406*, 213–222. https://doi.org/10.1016/j.epsl.2014.09.018

Bunge, H. (1982). Texture Analysis in Materials Science: Mathematical Methods. London: Butterworth and Co.

Bystricky, M., Kunze, K., Burlini, L., & Burg, J. (2000). High shear strain of olivine aggregates: rheological and seismic consequences. *Science*, *290*(5496), 1564–1567. https://doi.org/10.1126/science.290.5496.1564

Castelnau, O., Blackman, D. K., & Becker, T. W. (2009). Numerical simulations of texture development and associated rheological anisotropy in regions of complex mantle flow. *Geophysical Research Letters*, *36*(12), 851. https://doi.org/10.1029/2009GL038027

Chatzaras, V., Kruckenberg, S. C., Cohen, S. M., Medaris Jr., L. G., Withers, A. C., & Bagley, B. (2016) Axial-type olivine crystallographic preferred orientations: The effect of strain geometry on mantle texture. *Journal of Geophysical Research: Solid Earth*, *121*, 4895–4922. https://doi.org/10.1002/2015JB012628

Chin, E. J., Soustelle, V., Hirth, G., Saal, A. E., Kruckenberg, S. C., & Eiler, J. M. (2016). Microstructural and geochemical constraints on the evolution of deep arc lithosphere. *Geochemistry, Geophysics, Geosystems*, *17*(7), 2497–2521. https://doi.org/10.1002/2015GC006156

Davis, G. H. (1983). Shear-zone model for the origin of metamorphic core complexes. *Geology*, *11*(6), 342–347.

De Paola, N., Holdsworth, R. E., & Collettini, C. (2008). The Internal Structure of Dilational Stepovers in Regional Transtension Zones. *International Geology Review*, *50*(3), 291–304. https://doi.org/10.2747/0020-6814.50.3.291

Dick, H. J. B. (1977). Partial melting in the Josephine Peridotite; I, The effect on mineral composition and its consequence for geobarometry and geothermometry. *American Journal of Science*, *277*(7), 801–832. https://doi.org/10.2475/ajs.277.7.801

Di Leo, J. F., Wookey, J., Hammond, J. O. S., Kendall, J.-M., Kaneshima, S., Inoue, H., et al. (2012). Mantle flow in regions of complex tectonics: Insights from Indonesia. *Geochemistry, Geophysics, Geosystems*, *13*(12). https://doi.org/10.1029/2012GC004417

Drury, M. R. (2005). Dynamic recrystallization and strain softening of olivine aggregates in the laboratory and the lithosphere. In D. Gapais, J. P. Brun, & P. R. Cobbold (Eds.), *Deformation Mechanisms, Rheology, and Tectonics: from Minerals to the Lithosphere* (Vol. 243, pp. 143–158). Geological Society of London. https://doi.org/10.1144/GSL.SP.2005.243.01.11

Durham, W. B., & Goetze, C. (1977). Plastic flow of oriented single crystals of olivine: 1. Mechanical data. *Journal of Geophysical Research*, *82*(36), 5737–5753. https://doi.org/10.1029/JB082i036p05737

Garcia, M. O. (1982). Petrology of the Rogue River island-arc complex, Southwest Oregon. *American Journal of Science*, *282*(6), 783–807. https://doi.org/10.2475/ajs.282.6.783

Grant, K. J., Kohn, S. C., & Brooker, R. A. (2006). Solubility and partitioning of water in synthetic forsterite and enstatite in the system MgO–SiO2–H2O±Al2O3. *Contributions to Mineralogy and Petrology. Beitrage Zur Mineralogie Und Petrologie*, *151*(6), 651–664. https://doi.org/10.1007/s00410-006-0082-7

Hansen, L. N., & Warren, J. M. (2015). Quantifying the effect of pyroxene on deformation of peridotite in a natural shear zone. *Journal of Geophysical Research: Solid Earth*, *120*(4), 2717–2738. https://doi.org/10.1002/2014JB011584

Hansen, L. N., Zimmerman, M. E., & Kohlstedt, D. L. (2011). Grain boundary sliding in San Carlos olivine: Flow law parameters and crystallographic-preferred orientation. *Journal of Geophysical Research*, *116*(B8), 149. https://doi.org/10.1029/2011JB008220

Hansen, L. N., Zimmerman, M. E., & Kohlstedt, D. L. (2012). The influence of microstructure on deformation of olivine in the grain-boundary sliding regime. *Journal of Geophysical Research*, *117*(B9), 149. https://doi.org/10.1029/2012JB009305

Hansen, L. N., Zhao, Y. H., Zimmerman, M. E., & Kohlstedt, D. L. (2014). Protracted fabric evolution in olivine: Implications for the relationship among strain, crystallographic fabric, and seismic anisotropy. *Earth and Planetary Science Letters*, *387*, 157–168. https://doi.org/10.1016/j.epsl.2013.11.009

Hansen, L. N., Conrad, C. P., Boneh, Y., Skemer, P., Warren, J. M., & Kohlstedt, D. L. (2016). Viscous anisotropy of textured olivine aggregates: 2. Micromechanical model. *Journal of Geophysical Research: Solid Earth*, *121*(10), 7137–7160. https://doi.org/10.1002/2016JB013240

Hansen, L. N., Warren, J. M., Zimmerman, M. E., & Kohlstedt, D. L. (2016). Viscous anisotropy of textured olivine aggregates, Part 1: Measurement of the magnitude and evolution of anisotropy. *Earth and Planetary Science Letters*, *445*, 92–103. https://doi.org/10.1016/j.epsl.2016.04.008

Harding, D. J. (1988). *Josephine peridotite tectonites: A record of upper-mantle plastic flow* (Ph.D.). Cornell University.

Harper, G. D. (1984). The Josephine ophiolite, northwestern California. *GSA Bulletin*, *95*(9), 1009–1026. https://doi.org/2.0.CO;2">10.1130/0016-7606(1984)95<1009:TJONC>2.0.CO;2

Hauri, E. H., Gaetani, G., & Green, T. (2006). Partitioning of water during melting of the Earth’s upper mantle at H2O-undersaturated conditions. *Earth and Planetary Science Letters*, *248*(3-4), 715–734. https://doi.org/10.1016/j.epsl.2006.06.014

Herren, E. (1987). Zanskar shear zone: Northeast-southwest extension within the Higher Himalayas (Ladakh, India). *Geology*, *15*(5), 409–413. https://doi.org/2.0.CO;2">10.1130/0091-7613(1987)15<409:ZSZNEW>2.0.CO;2

Hess, H. H. (1964). Seismic Anisotropy of the Uppermost Mantle under Oceans. *Nature*, *203*, 629. https://doi.org/10.1038/203629a0

Himmelberg, G. R., & Loney, R. A. (1973). Petrology of the Vulcan Peak Alpine-Type Peridotite, Southwestern Oregon. *GSA Bulletin*, *84*(5), 1585–1600. https://doi.org/2.0.CO;2">10.1130/0016-

7606(1973)84<1585:POTVPA>2.0.CO;2

Holtzman, B. K., Kohlstedt, D. L., Zimmerman, M. E., Heidelbach, F., Hiraga, T., & Hustoft, J. (2003). Melt segregation and strain partitioning: implications for seismic anisotropy and mantle flow. *Science*, *301*(5637), 1227–1230. https://doi.org/10.1126/science.1087132

Humphreys, F. J., Bate, P. S., & Hurley, P. J. (2001). Orientation averaging of electron backscattered diffraction data. *Journal of Microscopy*, *201*(Pt 1), 50–58. https://doi.org/10.1046/j.1365-2818.2001.00777.x

Jung, H., & Karato, S.-I. (2001). Water-induced fabric transitions in olivine. *Science*, *293*(5534), 1460–1463. https://doi.org/10.1126/science.1062235

Jung, H., Katayama, I., Jiang, Z., Hiraga, T., & Karato, S.-I. (2006). Effect of water and stress on the lattice-preferred orientation of olivine. *Tectonophysics*, *421*(1), 1–22. https://doi.org/10.1016/j.tecto.2006.02.011

Karato, S.-I. (1989). Defects and plastic deformation in olivine. In S.-I. Karato & M. Toriumi (Eds.), *Rheology of Solids and of the Earth* (pp. 176–208).

Karato, S.-I., Toriumi, M., & Fujii, T. (1980). Dynamic recrystallization of olivine single crystals during high-temperature creep. *Geophysical Research Letters*, *7*(9), 649–652. https://doi.org/10.1029/GL007i009p00649

Karato, S.-I., Jung, H., Katayama, I., & Skemer, P. (2008). Geodynamic Significance of Seismic Anisotropy of the Upper Mantle: New Insights from Laboratory Studies. *Annual Review of Earth and Planetary Sciences*, *36*(1), 59–95. https://doi.org/10.1146/annurev.earth.36.031207.124120

Katayama, I., Jung, H., & Karato, S.-I. (2004). New type of olivine fabric from deformation experiments at modest water content and low stress. *Geology*, *32*(12), 1045–1048. https://doi.org/10.1130/G20805.1

Katayama, I., & Karato, S.-I. (2006) Effect of temperature on the B- to C-type olivine fabric transition and implication for flow pattern in subduction zones. *Physics of the Earth and Planetary Interiors,* *157*(1–2), 33–45. https://doi.org/10.1016/j.pepi.2006.03.005

Kelemen, P. B., & Dick, H. J. B. (1995). Focused melt flow and localized deformation in the upper mantle: Juxtaposition of replacive dunite and ductile shear zones in the Josephine peridotite, SW Oregon. *Journal of Geophysical Research*, *100*(B1), 423–438. https://doi.org/10.1029/94JB02063

Kumamoto, K. M., Warren, J. M., & Hauri, E. H. (in revison). Evolution of the Josephine Peridotite shear zones, Part 1: Compositional variation and shear initiation. *Geochemistry, Geophysics, Geosystems*.

Lloyd, G. E., Farmer, A. B., & Mainprice, D. (1997). Misorientation analysis and the formation and orientation of subgrain and grain boundaries. *Tectonophysics*, *279*(1), 55–78. https://doi.org/10.1016/S0040-1951(97)00115-7

Loney, R. A., & Himmelberg, G. R. (1976). Structure of the Vulcan Peak alpine-type peridotite, southwestern Oregon. *GSA Bulletin*, *87*(2), 259–274. https://doi.org/2.0.CO;2">10.1130/0016-7606(1976)87<259:SOTVPA>2.0.CO;2

Mackwell, S. J., Kohlstedt, D. L., & Paterson, M. S. (1985). The role of water in the deformation of olivine single crystals. *Journal of Geophysical Research*, *90*(B13), 11319. https://doi.org/10.1029/JB090iB13p11319

Mainprice, D., Tommasi, A., Couvy, H., Cordier, P., & Frost, D. J. (2005). Pressure sensitivity of olivine slip systems and seismic anisotropy of Earth's upper mantle. *Nature*, *433*(7027), 731–733. https://doi.org/10.1038/nature03266

Mainprice, D., Bachmann, F., Hielscher, R., & Schaeben, H. (2014). Descriptive tools for the analysis of texture projects with large datasets using MTEX: strength, symmetry and components. In D. R. Faulkner, E. Mariani, & J. Mecklenburgh (Eds.), *Rock Deformation from Field, Experiments, and Theory: A Volume in Honour of Ernie Rutter* (Vol. 409, pp. 251–271). Geological Society of London. https://doi.org/10.1144/SP409.8

Mehl, L., Hacker, B. R., Hirth, G., & Kelemen, P. B. (2003). Arc-parallel flow within the mantle wedge: Evidence from the accreted Talkeetna arc, south central Alaska. *Journal of Geophysical Research*, *108*(B8), 1–18. https://doi.org/10.1029/2002JB002233

Mercier, J.-C. C., Anderson, D. A., & Carter, N. L. (1977). Stress in the Lithosphere: Inferences from

Steady State Flow of Rocks. *Pure and Applied Geophysics*, *115*(1-2), 199–226. https://doi.org/10.1007/978-3-0348-5745-1_12

Nevitt, J. M., Warren, J. M., Kumamoto, K. M., & Pollard, D. D. (2019). Using geologic structures to constrain constitutive laws not accessible in the laboratory. *Journal of Structural Geology, 125, 55–63*. https://doi.org/10.1016/j.jsg.2018.06.006

Nevitt, J. M., Pollard, D. D., & Warren, J. M. (2014). Evaluation of transtension and transpression within contractional fault steps: Comparing kinematic and mechanical models to field data. *Journal of Structural Geology*, *60*, 55–69. https://doi.org/10.1016/j.jsg.2013.12.011

Nicolas, A., & Christensen, N. I. (1987). Formation of anisotropy in upper mantle peridotites: A review. In K. Fuchs & C. Froidevaux (Eds.), *Composition, Structure and Dynamics of the Lithosphere-Asthenosphere System* (Vol. 16, pp. 111–123). Washington, D. C.: American Geophysical Union. https://doi.org/10.1029/GD016p0111

Nicolas, A., Boudier, F., & Boullier, A. M. (1973). Mechanisms of flow in naturally and experimentally deformed peridotites. *American Journal of Science*, *273*(10), 853–876. https://doi.org/10.2475/ajs.273.10.853

O'Leary, J. A., Gaetani, G. A., & Hauri, E. H. (2010). The effect of tetrahedral Al3+ on the partitioning of water between clinopyroxene and silicate melt. *Earth and Planetary Science Letters*, *297*(1), 111–120. https://doi.org/10.1016/j.epsl.2010.06.011

Paterson, M. S. (1982). The determination of hydroxyl by infrared adsorption in quartz, silicate glasses and similar materials. *Bulletin de Mineralogie*, *105*, 20–29.

Peslier, A. H. (2010). A review of water contents of nominally anhydrous natural minerals in the mantles of Earth, Mars and the Moon. *Journal of Volcanology and Geothermal Research*, *197*(1), 239–258. https://doi.org/10.1016/j.jvolgeores.2009.10.006

Qi, C., Hansen, L. N., Wallis, D., Holtzman, B. K., & Kohlstedt, D. L. (2018). Crystallographic Preferred Orientation of Olivine in Sheared Partially Molten Rocks: The Source of the "a-c Switch." *Geochemistry, Geophysics, Geosystems*, *19*(2), 316–336. https://doi.org/10.1002/2017GC007309

Ramsay, J. G. (1980). Shear zone geometry: A review. *Journal of Structural Geology*, *2*(1), 83–99. https://doi.org/10.1016/0191-8141(80)90038-3

Ramsay, J. G., & Graham, R. H. (1970). Strain variation in shear belts. Canadian Journal of Earth Sciences, 7(3), 786–813. https://doi.org/10.1139/e70-078

Recanati, A., Kurz, M. D., Warren, J. M., & Curtice, J. (2012). Helium distribution in a mantle shear zone from the Josephine Peridotite. *Earth and Planetary Science Letters*, *359-360*, 162–172. https://doi.org/10.1016/j.epsl.2012.09.046

Saleeby, J. B., Harper, G. D., Snoke, A. W., & Sharp, W. D. (1982). Time relations and structural-stratigraphic patterns in ophiolite accretion, west central Klamath Mountains, California. *Journal of Geophysical Research*, *87*(B5), 3831. https://doi.org/10.1029/JB087iB05p03831

Signorelli, J., & Tommasi, A. (2015). Modeling the effect of subgrain rotation recrystallization on the evolution of olivine crystal preferred orientations in simple shear. *Earth and Planetary Science Letters*, *430*, 356–366. https://doi.org/10.1016/j.epsl.2015.08.018

Skemer, P., & Hansen, L. N. (2016). Inferring upper-mantle flow from seismic anisotropy: An experimental perspective. *Tectonophysics*, *668-669*, 1–14. https://doi.org/10.1016/j.tecto.2015.12.003

Skemer, P., Katayama, I., Jiang, Z., & Karato, S.-I. (2005). The misorientation index: Development of a new method for calculating the strength of lattice-preferred orientation. *Tectonophysics*, *411*(1), 157–167. https://doi.org/10.1016/j.tecto.2005.08.023

Skemer, P., Warren, J. M., Kelemen, P. B., & Hirth, G. (2010). Microstructural and Rheological Evolution of a Mantle Shear Zone. *Journal of Petrology*, *51*(1-2), 43–53. https://doi.org/10.1093/petrology/egp057

Skemer, P., Warren, J. M., & Hirth, G. (2012). The influence of deformation history on the interpretation of seismic anisotropy. *Geochemistry, Geophysics, Geosystems*, *13*(3). https://doi.org/10.1029/2011GC003988

Skemer, P., Warren, J. M., Hansen, L. N., Hirth, G., & Kelemen, P. B. (2013). The influence of water and

LPO on the initiation and evolution of mantle shear zones. *Earth and Planetary Science Letters*, *375*, 222–233. https://doi.org/10.1016/j.epsl.2013.05.034

Tasaka, M., Zimmerman, M. E., & Kohlstedt, D. L. (2017). Rheological Weakening of Olivine + Orthopyroxene Aggregates Due to Phase Mixing: 1. Mechanical Behavior. *Journal of Geophysical Research: Solid Earth*, *122*(10), 7584–7596. https://doi.org/10.1002/2017JB014333

Tenner, T. J., Hirschmann, M. M., Withers, A. C., & Hervig, R. L. (2009). Hydrogen partitioning between nominally anhydrous upper mantle minerals and melt between 3 and 5 GPa and applications to hydrous peridotite partial melting. *Chemical Geology*, *262*(1), 42–56. https://doi.org/10.1016/j.chemgeo.2008.12.006

Tommasi, A., Tikoff, B., & Vauchez, A. (1999). Upper mantle tectonics: three-dimensional deformation, olivine crystallographic fabrics and seismic properties. *Earth and Planetary Science Letters*, *168*(1), 173–186. https://doi.org/10.1016/S0012-821X(99)00046-1

Tommasi, A., Mainprice, D., Canova, G., & Chastel, Y. (2000). Viscoplastic self-consistent and equilibrium-based modeling of olivine lattice preferred orientations: Implications for the upper mantle seismic anisotropy. *Journal of Geophysical Research*, *105*(B4), 7893–7908. https://doi.org/10.1029/1999JB900411

Toriumi, M. (1979). Relation between dislocation density and subgrain size of naturally deformed olivine in peridotites. *Contributions to Mineralogy and Petrology. Beitrage Zur Mineralogie Und Petrologie*, *68*(2), 181–186. https://doi.org/10.1007/BF00371899

Twiss, R. J. (1977). Theory and Applicability of a Recrystallized Grain Size Paleopiezometer. *Pure and Applied Geophysics*, *115*(1-2), 227–244. https://doi.org/10.1007/978-3-0348-5745-1_13

Underwood, E. E. (1970). *Quantitative stereology*. Addison-Wesley Publishing Company.

Van der Wal, D., Chopra, P., Drury, M., & Gerald, J. F. (1993). Relationships between dynamically recrystallized grain size and deformation conditions in experimentally deformed olivine rocks. *Geophysical Research Letters*, *20*(14), 1479–1482. https://doi.org/10.1029/93GL01382

Warren, J. M., & Hauri, E. H. (2014). Pyroxenes as tracers of mantle water variations. *Journal of*

Geophysical Research: Solid Earth, *119*(3), 1851–1881. https://doi.org/10.1002/2013JB010328

Warren, J. M., & Hirth, G. (2006). Grain size sensitive deformation mechanisms in naturally deformed peridotites. *Earth and Planetary Science Letters*, *248*(1), 438–450. https://doi.org/10.1016/j.epsl.2006.06.006

Warren, J. M., Hirth, G., & Kelemen, P. B. (2008). Evolution of olivine lattice preferred orientation during simple shear in the mantle. *Earth and Planetary Science Letters*, *272*(3), 501–512. https://doi.org/10.1016/j.epsl.2008.03.063

Woodcock, N. H. (1977). Specification of fabric shapes using an eigenvalue method. *GSA Bulletin*, *88*(9), 1231–1236. https://doi.org/2.0.CO;2">10.1130/0016-7606(1977)88<1231:SOFSUA>2.0.CO;2

Zeuch, D. H., & Green, H. W., II. (1984). Experimental deformation of a synthetic dunite at high temperature and pressure. I. Mechanical behavior, optical microstructure and deformation mechanism. *Tectonophysics*, *110*(3), 233–262. https://doi.org/10.1016/0040-1951(84)90263-4

Zhang, S., & Karato, S.-I. (1995). Lattice preferred orientation of olivine aggregates deformed in simple shear. *Nature*, *375*, 774. https://doi.org/10.1038/375774a0

Zhang, S., Karato, S.-I., Fitz Gerald, J., Faul, U. H., & Zhou, Y. (2000). Simple shear deformation of olivine aggregates. *Tectonophysics*, *316*(1), 133–152. https://doi.org/10.1016/S0040-1951(99)00229-2